Imaging Agents Hot Paper

International Edition: DOI: 10.1002/anie.201507473
German Edition: DOI: 10.1002/ange.201507473

Fluorescence Imaging In Vivo at Wavelengths beyond 1500 nm

*Shuo Diao, Jeffrey L. Blackburn, Guosong Hong, Alexander L. Antaris, Junlei Chang, Justin Z. Wu, Bo Zhang, Kai Cheng, Calvin J. Kuo, and Hongjie Dai**

Abstract: *Compared to imaging in the visible and near-infrared regions below 900 nm, imaging in the second near-infrared window (NIR-II, 1000–1700 nm) is a promising method for deep-tissue high-resolution optical imaging in vivo mainly owing to the reduced scattering of photons traversing through biological tissues. Herein, semiconducting single-walled carbon nanotubes with large diameters were used for in vivo fluorescence imaging in the long-wavelength NIR region (1500–1700 nm, NIR-IIb). With this imaging agent, 3–4 μm wide capillary blood vessels at a depth of about 3 mm could be resolved. Meanwhile, the blood-flow speeds in multiple individual vessels could be mapped simultaneously. Furthermore, NIR-IIb tumor imaging of a live mouse was explored. NIR-IIb imaging can be generalized to a wide range of fluorophores emitting at up to 1700 nm for high-performance in vivo optical imaging.*

Fluorescence-based optical imaging is indispensable to investigating biological systems with high spatial and temporal resolution.[1] However, a formidable challenge to in vivo fluorescence imaging of live animals has been the limited depth of penetration and inability of high-resolution imaging through live tissues owing to both the absorption and scattering of photons. To circumvent this problem, we and others have recently explored in vivo fluorescence imaging in the second near-infrared window (NIR-II, 1000–1700 nm) to benefit from reduced photon scattering and achieve higher imaging resolution deeper in the body than with traditional NIR imaging (NIR-I, 750–900 nm).[2] Nevertheless, the NIR-II fluorophores used thus far mainly emit below about 1400 nm, which is still not optimal from the tissue scattering point of view. Although in vivo fluorescence imaging at longer wavelengths would further reduce scattering, increased water absorption upon approaching the infrared region could diminish the intensity of light passing through biological tissues, which is a valid concern that has deterred in vivo fluorescence imaging in the long-wavelength NIR region. Another consideration for the development of in vivo fluorescence imaging in the long NIR window is the lack of biocompatible emitters with sufficient brightness. To date, most NIR-II in vivo fluorescence imaging has been based on high-pressure carbon monoxide conversion (HiPCO) single-walled nanotubes (SWNTs) with a small diameter distribution of 0.7–1.1 nm, emitting band-gap fluorescence in the range of 1000–1400 nm.[2c,g,h,3] We expect that SWNTs with larger diameters, such as SWNTs grown by the laser vaporization method originally developed by Smalley,[4] could enable high-resolution fluorescence imaging in the longer-wavelength region.

The long-wavelength NIR-II region near 1600 nm offers a balance of photon-scattering and water-absorption effects, promising to significantly enhance the performance of fluorescence imaging in vivo, by achieving both improved penetration depth and imaging resolution. As shown in the

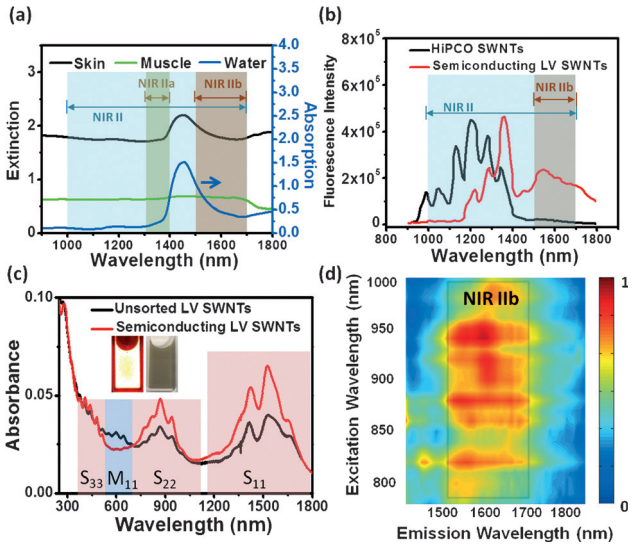

Figure 1. Semiconducting LV SWNTs for fluorescence imaging in the NIR-IIb region. a) Optical absorption spectrum of water and extinction spectra of mouse skin and mouse muscle. b) NIR fluorescence spectra of HiPCO and semiconducting LV SWNTs upon 808 nm excitation. c) Optical absorption spectra of pristine and separated semiconducting LV SWNTs. Photoluminescence (inset, left) and optical (inset, right) images of semiconducting LV SWNTs are also shown. d) The photoluminescence versus excitation (PLE) map of semiconducting LV SWNTs shows bright emission in the NIR-IIb region.

[*] S. Diao,[+] Dr. G. Hong,[+] A. L. Antaris, Dr. J. Z. Wu, B. Zhang, Prof. H. Dai
Department of Chemistry, Stanford University
Stanford, California 94305 (USA)
E-mail: hdai@stanford.edu

Dr. J. L. Blackburn[+]
Chemical and Materials Science Center
National Renewable Energy Laboratory
Golden, Colorado 80401 (USA)

Dr. J. Chang, Prof. C. J. Kuo
Division of Hematology, School of Medicine
Stanford University
Stanford, California 94305 (USA)

Dr. K. Cheng
Department of Radiology and Bio-X Program
School of Medicine, Stanford University
Stanford, California 94305 (USA)

[+] These authors contribute to the work equally.

Supporting information for this article is available on the WWW under http://dx.doi.org/10.1002/anie.201507473.

absorption spectrum of water and the extinction spectra of biological tissues (Figure 1a), the near 1600 nm region resides in a local valley between a water vibrational OH stretching overtone absorption peak at approximately 1450 nm and the edge of an increasing water absorption combination band beyond 1700 nm. Thus, the fluorescence imaging window near 1600 nm offers a local minimum in the water absorption spectrum to minimize attenuation of the fluorescence signal caused by water dominant in biological tissues. On the other hand, as photon scattering scales as $\lambda^{-\alpha}$ ($\alpha = 0.2$–4 for different tissues),[5] the near 1600 nm window provides the lowest photon scattering in the entire NIR-II window (without water absorption dominance), useful for high-resolution, deep-tissue biological imaging.

We herein report the successful in vivo fluorescence imaging (under 808 nm excitation) in the 1500–1700 nm NIR-II window (referred to as the "NIR-IIb" window). Semiconducting SWNTs with improved fluorescence brightness are chemically enriched from unsorted SWNTs synthesized by laser vaporization. The NIR-IIb imaging window affords an in vivo vascular imaging spatial resolution down to approximately 4 μm at a depth of up to about 3 mm in the mouse hindlimb and brain with intact skull and scalp. Simultaneous single-vessel-resolved blood-flow speed mapping for multiple hindlimb arterial vessels is achieved by video-rate fluorescence imaging in the NIR-IIb region. Furthermore, high-performance NIR-IIb tumor imaging with clear and sharp resolution is explored.

The SWNT NIR-IIb emitters with a diameter range of approximately 0.96–1.24 nm were synthesized by laser vaporization (LV).[6] Changing the furnace temperature during LV synthesis from 950 °C to 1125 °C changed the SWNT average diameter from approximately 0.9 to 1.4 nm, allowing us to identify the SWNTs grown at 950 °C to be the brightest for imaging in the NIR-IIb window (Supporting Information, Figure S1). Compared to the previously widely used HiPCO SWNTs, the LV nanotubes exhibited higher fluorescence in the 1500–1700 nm region owing to the smaller band gaps and the larger average diameter (Figure S2; quantum yield measurements are shown in Figure S3).[4b] The LV SWNTs grown at 950 °C were then suspended by sonication and sorted through a chromatography column to enrich the semiconducting SWNTs (see the Method Section in the Supporting Information).[2a,7] Compared to the raw material, the resulting semiconducting LV SWNTs exhibited enhanced S_{11}/S_{22} (ca. 700–1800 nm) peaks and reduced M_{11} peaks (ca. 500–700 nm) in the UV/Vis/NIR absorption spectra (Figure 1c), indicating successful enrichment of the semiconducting LV SWNTs needed for biological imaging with sufficiently bright fluorescence in the NIR-IIb window (Figure 1b,d).

The semiconducting enriched LV SWNTs were stably suspended in aqueous biological solutions with highly biocompatible surface coatings by employing an exchange functionalization method (see the Supporting Information).[2g] We evaluated the wavelength-dependent non-invasive fluorescence imaging of mouse brain vessels at depths of up to 3 mm through the intact scalp and skull of C57Bl/6 mice (after shaving to remove hair) by intravenously injecting indocyanine green (ICG, emitting in the NIR-I region) or a mixture of biocompatible HiPCO and semiconducting LV SWNTs (Figure 2a–c). The images were recorded using a liquid-nitrogen-cooled 2D InGaAs camera (Princeton Instruments, detection range below ca. 1700 nm), which showed quantum efficiencies below 30% at wavelengths above 1600 nm;[8] therefore, most of the NIR-IIb signals recorded in this work were within the 1500–1600 nm region. We measured the signal-to-background ratios (SBRs) by plotting the cross-sectional intensity profiles of the same vessel imaged in the NIR-I (850-900 nm), NIR-II (1000–1700 nm), and NIR-IIb (1500–1700 nm) windows (Figure 2d–f). The SBR obtained by imaging in the NIR-IIb window was found to be higher than for the NIR-I and NIR-II windows (4.50 in NIR-IIb vs. 2.01 in NIR-II and 1.19 in NIR-I), suggesting that in vivo imaging beyond 1500 nm benefits from increased signal-to-background ratios. We also compared the photon scattering effects in the NIR-II and NIR-IIb windows and a previously defined NIR-IIa region (1300–1400 nm; Figure 1a)[2b] by performing phantom studies using both chicken breast (Figure S4) and intralipid (a scattering medium; Figure S5), showing the benefit of minimized photon scattering in the long-wavelength NIR-IIb region for fluorescence imaging with deep penetration.

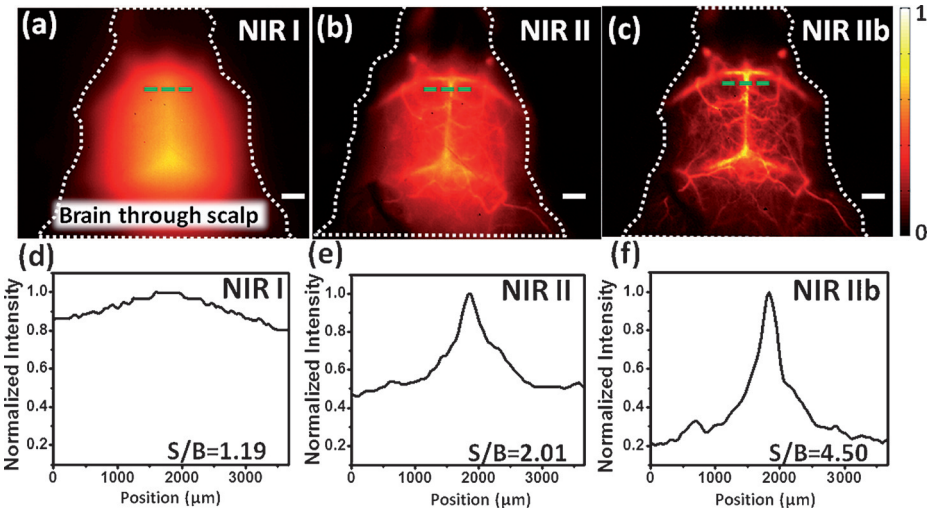

Figure 2. Fluorescence images of the cerebrovasculature of mice ($n = 2$) without craniotomy in the NIR-I (a), NIR-II (b), and NIR-IIb (c) regions, with the corresponding SBR analysis shown in (d)–(f). Scale bars: 2 mm.

We also performed high-magnification microscopic vessel imaging of both mouse hindlimb and brain with a pixel size of 2.5 μm in the NIR-IIa and NIR-IIb regions. By measuring the Gaussian-fitted full width at half maximum (FWHM) of the cross-sectional intensity profiles of the features, we found that the apparent widths of the same hindlimb blood vessel imaged at a depth of approximately 3 mm in the NIR-IIa (marked by a green line, Figure 3a) and NIR-IIb (marked by a green line, Figure 3b) were 9.7 μm and 6.3 μm, respectively, suggesting an improved spatial resolution in the longer-wavelength NIR-IIb window (Figure 3c). Also, we evaluated the SBRs of a blood vessel (marked by white lines, Figure 3a,b) imaged in both windows. A higher SBR of 3.85 was obtained in the NIR-IIb than in the NIR-IIa window (1.56) for the same blood vessel (Figure 3d). The smallest vessel resolved by NIR-IIb fluorescence imaging in the mouse hindlimb showed an apparent width (i.e., FWHM) of approximately 3.7 μm at a depth of about 2.6 mm (Figure 3e,f).

We then compared the performance of high-magnification cerebrovascular imaging in the NIR-IIa[2b] and NIR-IIb regions. Many vessels imaged in the NIR-IIb window showed generally improved feature sharpness (Figure 3i; FWHM ca. 5.4 μm in NIR-IIb vs. ca. 9.4 μm in NIR-IIa for the same blood vessel; green lines in Figure 3g,h) and increased SBRs (Figure 3j; 7.44 in NIR-IIb vs. 4.91 in NIR-IIa for the same vessel; white lines in Figure 3g,h). A small vessel with a FWHM width down to about 4 μm was measured in the NIR-IIb region at a depth of approximately 2.8 mm through the intact scalp and skull, achieving micrometer resolution for in vivo brain fluorescence imaging at >2 mm depth (Figure 3k,l). The imaging depth was determined throughout this work by recording the vertical axis travel distance of the microscopic objective with the surface of the skin set to be a depth of zero. Ex vivo mouse tissue imaging was also performed to study the scattering effects in vessel size measurements in the NIR-IIb region (Figure S6).

To perform video-rate fluorescence imaging of blood vessels in the mouse hindlimb in the NIR-IIb region, we injected a 200 μL solution of exchanged semiconducting LV SWNTs into the tail vein of an athymic nude mouse and performed NIR-IIb fluorescence imaging at a speed of 4.6 frames per second (Movie S1). Upon injection, blood flow into the femoral artery was clearly observed by video-rate imaging (Figure 4a). Aside from the main femoral artery, blood flow into numerous smaller, high-order arterial vessel branches was also observed (Figure 4b,c and Movie S1). These smaller vessels were deeper in the body than the femoral artery and were difficult to resolve by imaging in the 1000–1400 nm[2c] or 1500-1700 nm (Figure S7) range using HiPCO SWNTs. The blood-flow speeds in various arterial vessels were quantified from video-rate imaging (Movie S1) by plotting the distance travelled by the signal front versus time (Figure S8),[2c] affording a spatially resolved blood flow map showing blood flow speeds of approximately 22.6 mm s^{-1} in the femoral artery and 1.1 to 4.8 mm s^{-1} in the smaller arterial branches (Figure 4f). To the best of our knowledge,

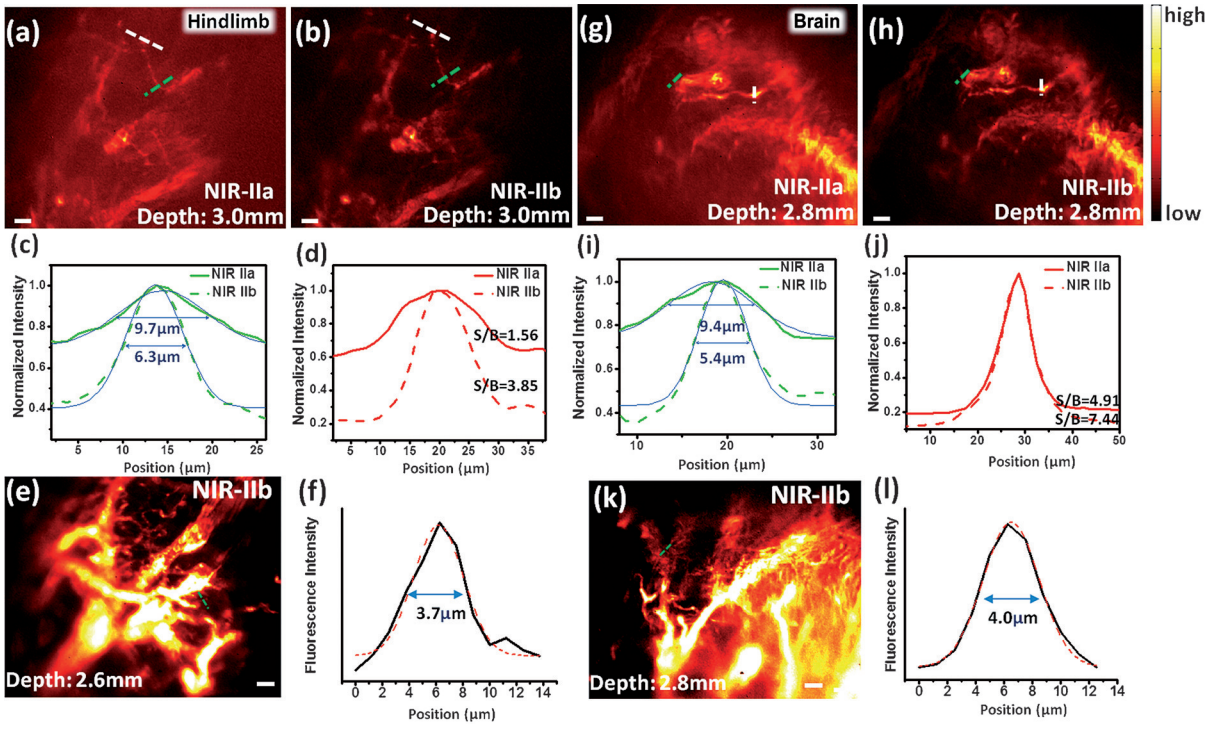

Figure 3. High-magnification vessel imaging of the hindlimb and brain of mice in the NIR-IIa and IIb windows. a,b) High-magnification microscopic images of the hindlimb vessels ($n=2$) at an imaging focal depth of 3 mm taken in the NIR-IIa and NIR-IIb windows, with the vessel FWHM width (green lines in a,b) and SBR (white lines in a,b) analysis shown in (c) and (d), respectively. The background signals for the SBR analysis were evaluated by averaging the baseline signals in the cross-sectional intensity profiles. e,f) A small blood vessel resolved by imaging in the NIR-IIb region. Similar vessel width and SBR analysis of the high-magnification cerebrovascular images in the NIR-IIa (g) and NIR-IIb (h) regions are shown in (i) and (j). k,l) A NIR-IIb fluorescence cerebrovascular image resolving a small vessel. Scale bars: 40 μm.

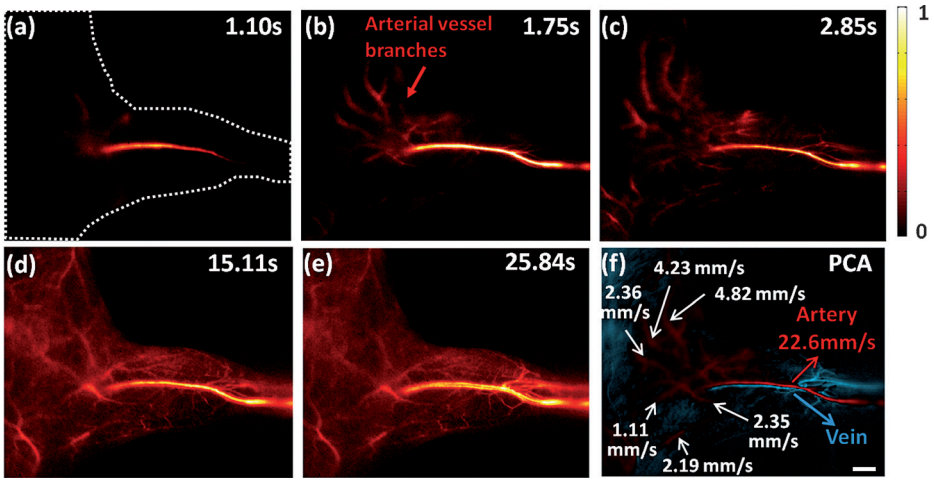

Figure 4. Video-rate NIR-IIb fluorescence imaging of mouse hindlimb vessels ($n=3$) and dynamic-contrast-based vessel type differentiation. a–e) Time-course NIR-IIb hindlimb fluorescence images after injection of semiconducting LV SWNTs into the tail vein of an athymic nude mouse. f) PCA overlaid image showing the differentiation of arterial (red) and venous (blue) vessels. The blood-flow velocities in the femoral artery and small, higher-order arterial vessels are also given. Scale bar: 2 mm.

this is the first time that blood flow velocities over a broad range of 1–20 mm s^{-1} in multiple vessels of mice were mapped simultaneously. Blood flow velocimetry over such a broad dynamic range from about 1 mm s^{-1} to >20 mm s^{-1} with spatially resolved individual vessels is hard to achieve with other standard techniques, such as laser Doppler and ultrasonography, which suffer from low spatial resolution, speckle artifacts, and a small dynamic range.[2c,3c,9]

The femoral veins were observed at about 26 s post injection (p.i.; Figure 4e), as these vessel structures became fluorescent in the NIR-IIb region owing to the blood flow completing a systemic circulation cycle in the hindlimb. Principal component analysis (PCA) of the video-rate image frames was performed to group the image pixels with similar time variance into distinct components, clearly identifying the various arterial branches and differentiating them from the venous vessels (Figure 4f).[2c,3a,10]

Lastly, we explored the NIR-IIb emitting SWNTs for in vivo tumor imaging. After intravenously injecting exchanged semiconducting LV SWNTs into a balb/c mouse bearing two subcutaneous 4T1 murine breast tumors, we performed video-rate (4.6 frames per second) NIR-IIb fluorescence imaging of the mouse under 808 nm excitation (Movie S2). Because of the pulmonary circulation, an intensity spike in the lungs (a deep organ in mice) was clearly resolved after injection into the tail vein (Figure 5b,c).

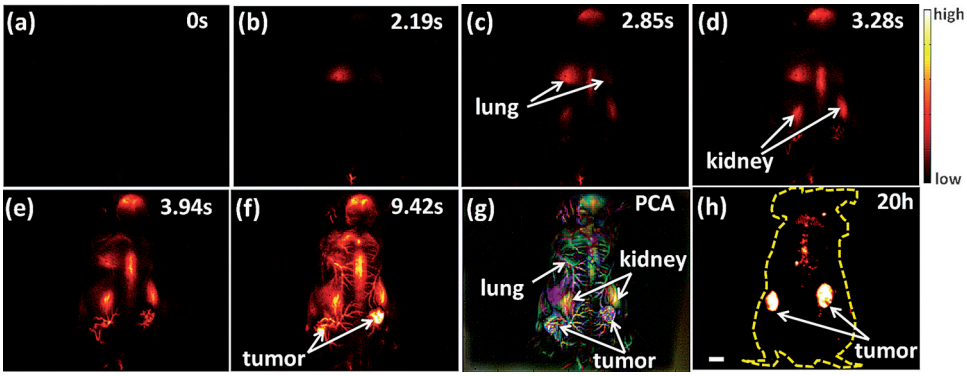

Figure 5. In vivo video-rate NIR-IIb tumor imaging in live mice ($n=2$). a–f) Time-course NIR-IIb fluorescence images of the tumor-bearing mice after intravenous injection of exchanged semiconducting LV SWNTs. g) Overlaid PCA image of the early image frames differentiating inner organs and the vascular structures surrounding tumors. h) A NIR-IIb fluorescence image of the tumor-bearing mouse taken at 20 h p.i., showing the high uptake in the tumor area that is due to the EPR effect. Scale bar: 4 mm.

Afterwards, NIR-IIb signals in the major organs (such as the kidneys) in the systemic circulation were clearly observed (Figure 5d,e). The vascular structures surrounding the tumors started to appear in a prominent manner at about 3.9 s p.i. (Figure 5e,f). These deep vessels were difficult to clearly resolve by imaging in shorter-wavelength regions owing to scattering by muscles and other tissues atop (Figure S10).[3b] Registration of the inner organs and vessels was evident by applying PCA to the frames of the video-rate movie (Figure 5g). Over the SWNT blood circulation (half-life of about 5.6 h; Figure S11),[11] the nanotubes gradually accumulated within the tumors owing to the enhanced permeability and retention (EPR) effect (Figure 5h).[3b,12] Aside from tumor uptake, the SWNTs were mainly accumulated in the liver and spleen of the reticuloendothelial system (RES) at seven days post injection (Figure S11).

In conclusion, we have shown that the long-wavelength NIR imaging window of 1500–1700 nm is advantageous for in vivo fluorescence imaging as photon scattering is minimized. Water absorption is slightly higher in the NIR-IIb than in the traditional NIR window, but the absorption effects can be overcome with sufficiently bright fluorophores. This is an approach worth taking as scattering problems cannot be easily solved or avoided unless longer-wavelength photons are detected. NIR-IIb imaging offers the lowest light scattering among all the NIR sub-regions examined, affording high spatial resolution, deep tissue penetration, and high signal/background ratios for in vivo biological imaging. The results

here are not limited to nanotube fluorophores, and should be generalized to other agents emitting in the region up to 1700 nm, especially for fluorophores with much higher quantum yields, for further enhancing NIR-IIb imaging capabilities.

Keywords: cancer · fluorescence · imaging agents · nanotechnology · near infrared

How to cite: *Angew. Chem. Int. Ed.* **2015**, *54*, 14758–14762
Angew. Chem. **2015**, *127*, 14971–14975

[1] a) J. V. Frangioni, *Curr. Opin. Chem. Biol.* **2003**, *7*, 626; b) S. A. Hilderbrand, R. Weissleder, *Curr. Opin. Chem. Biol.* **2010**, *14*, 71; c) X. Le Guével, C. Spies, N. Daum, G. Jung, M. Schneider, *Nano Res.* **2012**, *5*, 379; d) T. Yang, Q. Liu, S. Pu, Z. Dong, C. Huang, F. Li, *Nano Res.* **2012**, *5*, 494.

[2] a) S. Diao, G. Hong, J. T. Robinson, L. Jiao, A. L. Antaris, J. Z. Wu, C. L. Choi, H. Dai, *J. Am. Chem. Soc.* **2012**, *134*, 16971; b) G. Hong, S. Diao, J. Chang, A. L. Antaris, C. Chen, B. Zhang, S. Zhao, D. N. Atochin, P. L. Huang, K. I. Andreasson, *Nat. Photonics* **2014**, *8*, 723; c) G. Hong, J. C. Lee, J. T. Robinson, U. Raaz, L. Xie, N. F. Huang, J. P. Cooke, H. Dai, *Nat. Med.* **2012**, *18*, 1841; d) G. Hong, Y. Zou, A. L. Antaris, S. Diao, D. Wu, K. Cheng, X. Zhang, C. Chen, B. Liu, Y. He, *Nat. Commun.* **2014**, *5*, 4206; e) D. Naczynski, M. Tan, M. Zevon, B. Wall, J. Kohl, A. Kulesa, S. Chen, C. Roth, R. Riman, P. Moghe, *Nat. Commun.* **2013**, *4*, 2199; f) A. M. Smith, M. C. Mancini, S. Nie, *Nat. Nanotechnol.* **2009**, *4*, 710; g) K. Welsher, Z. Liu, S. P. Sherlock, J. T. Robinson, Z. Chen, D. Daranciang, H. Dai, *Nat. Nanotechnol.* **2009**, *4*, 773; h) H. Yi, D. Ghosh, M.-H. Ham, J. Qi, P. W. Barone, M. S. Strano, A. M. Belcher, *Nano Lett.* **2012**, *12*, 1176.

[3] a) K. Welsher, S. P. Sherlock, H. J. Dai, *Proc. Natl. Acad. Sci. USA* **2011**, *108*, 8943; b) J. T. Robinson, G. Hong, Y. Liang, B. Zhang, O. K. Yaghi, H. Dai, *J. Am. Chem. Soc.* **2012**, *134*, 10664; c) G. Hong, J. C. Lee, A. Jha, S. Diao, K. H. Nakayama, L. Hou, T. C. Doyle, J. T. Robinson, A. L. Antaris, H. Dai, *Circ.: Cardiovasc. Imaging* **2014**, *7*, 517.

[4] a) T. Guo, P. Nikolaev, A. Thess, D. Colbert, R. Smalley, *Chem. Phys. Lett.* **1995**, *243*, 49; b) S. M. Bachilo, M. S. Strano, C. Kittrell, R. H. Hauge, R. E. Smalley, R. B. Weisman, *Science* **2002**, *298*, 2361; c) M. J. O'Connell, S. M. Bachilo, C. B. Huffman, V. C. Moore, M. S. Strano, E. H. Haroz, K. L. Rialon, P. J. Boul, W. H. Noon, C. Kittrell, J. Ma, R. H. Hauge, R. B. Weisman, R. E. Smalley, *Science* **2002**, *297*, 593.

[5] A. Bashkatov, E. Genina, V. Kochubey, V. Tuchin, *J. Phys. D* **2005**, *38*, 2543.

[6] K. S. Mistry, B. A. Larsen, J. L. Blackburn, *ACS Nano* **2013**, *7*, 2231.

[7] Y. Miyata, K. Shiozawa, Y. Asada, Y. Ohno, R. Kitaura, T. Mizutani, H. Shinohara, *Nano Res.* **2011**, *4*, 963.

[8] Princeton Instruments, 2D-OMA V InGaAs camera user manual.

[9] a) J. W. Xuan, M. Bygrave, H. Jiang, F. Valiyeva, J. Dunmore-Buyze, D. W. Holdsworth, J. I. Izawa, G. Bauman, M. Moussa, S. F. Winter, *Cancer Res.* **2007**, *67*, 2830; b) K. Z. Abd-Elmoniem, A. Youssef, Y. M. Kadah, *Biomed. Eng. IEEE Trans.* **2002**, *49*, 997.

[10] E. M. Hillman, A. Moore, *Nat. Photonics* **2007**, *1*, 526.

[11] Z. Liu, C. Davis, W. Cai, L. He, X. Chen, H. Dai, *Proc. Natl. Acad. Sci. USA* **2008**, *105*, 1410.

[12] A. K. Iyer, G. Khaled, J. Fang, H. Maeda, *Drug Discovery Today* **2006**, *11*, 812.

Received: August 11, 2015
Published online: October 13, 2015

